

Structure of rapidly quenched $(\text{Cu}_{0.5}\text{Zr}_{0.5})_{100-x}\text{Ag}_x$ alloys ($x = 0\text{--}40\text{ at.}\%$)

N. Mattern^{a,*}, J.H. Han^a, K.G. Pradeep^b, K.C. Kim^c, E.M. Park^a, D.H. Kim^c, Y. Yokoyama^d, D. Raabe^b, J. Eckert^{a,e}

^a IFW Dresden, Institute for Complex Materials, Helmholtzstr. 20, 01069 Dresden, Germany

^b Max-Planck-Institut für Eisenforschung GmbH, Max-Planck-Straße 1, 40237 Düsseldorf, Germany

^c Center for Non-crystalline Materials, Yonsei University, 134 Shinchon-dong, Seodaemun-ku, Seoul 120-749, Republic of Korea

^d Institute for Materials Research, Tohoku University, Sendai 980-8577, Japan

^e TU Dresden, Institute of Materials Science, Helmholtzstr. 7, 01069 Dresden, Germany

ARTICLE INFO

Article history:

Received 13 March 2014

Received in revised form 4 April 2014

Accepted 7 April 2014

Available online 18 April 2014

Keywords:

Metallic glass

Phase separation

Atom Probe Tomography

Ag–Cu–Zr

ABSTRACT

The influence of Ag addition on the microstructure of rapidly quenched $(\text{Cu}_{0.5}\text{Zr}_{0.5})_{100-x}\text{Ag}_x$ melts was investigated ($x = 0\text{--}40\text{ at.}\%$). Fully glassy alloys were obtained for $0 \leq x \leq 20\text{ at.}\%$ Ag, which are characterized by a homogeneous microstructure without any indication of phase separation. For $30 \leq x \leq 40\text{ at.}\%$ Ag a composite structure is formed consisting of *fcc*-Ag nano-crystallites 5 nm in size and an amorphous matrix phase $\text{Cu}_{40}\text{Zr}_{40}\text{Ag}_{20}$. With higher Ag-content the volume fraction of the *fcc*-Ag phase becomes increased mainly due to crystal growth during quenching. The primary formation of *fcc*-Ag for $30 \leq x \leq 40\text{ at.}\%$ Ag is confirmed by the analysis of the microstructure of mold cast bulk samples which were fully crystalline. From the experimental results we conclude that the miscibility gap of the liquid phase of the ternary Ag–Cu–Zr system may occur only for $x > 40\text{ at.}\%$ Ag. For the bulk glass forming quaternary $\text{Cu}_{40}\text{Zr}_{40}\text{Al}_{10}\text{Ag}_{10}$ alloy a homogeneous element distribution is observed in accordance with the microstructure of ternary $(\text{Cu}_{0.5}\text{Zr}_{0.5})_{100-x}\text{Ag}_x$ glasses ($x = 10, 20\text{ at.}\%$).

© 2014 Elsevier B.V. All rights reserved.

1. Introduction

Bulk metallic glasses (BMGs) exhibit excellent mechanical properties such as high strength and large elastic strain, making them attractive for structural applications [1]. Among them, Cu–Zr based BMGs demonstrate a high potential of having industrial applications in the future owing to their high strength, hardness, wear resistance, casting ability and high glass-forming ability. Recently, Cu–Zr–Al–Ag bulk glass forming alloys were developed with a critical diameter up to 25 mm for copper mould casting [2–4]. Bulk glass formation was also observed for ternary Cu–Zr–Ag alloys with a critical diameter up to 6 mm for $\text{Cu}_{45}\text{Zr}_{45}\text{Ag}_{10}$ [5,6]. For some Cu–Zr–Al–Ag BMGs also extended plasticity in compression and even in bending was reported [2,7]. However, the structural reason behind the deformability is not known so far. The presence of nanometer-scale phase separation was detected for a $\text{Cu}_{43}\text{Zr}_{43}\text{Al}_7\text{Ag}_7$ BMG (2 mm in thickness) by Atom Probe Tomography (APT) and was related to the extended plasticity [8]. Possible phase separation of submicron-scale upon annealing is discussed for glassy $\text{Cu}_{35}\text{Zr}_{45}\text{Ag}_{20}$ by a systematic study of the devitrification

and glass-forming ability of rapidly quenched Cu–Zr–Ag alloys [9]. The same group has also reported the occurrence of possible phase separation for a $\text{Zr}_{48}\text{Cu}_{36}\text{Al}_8\text{Ag}_8$ BMG (3 mm in thickness) in the supercooled liquid state just prior to crystallization [10]. On the other side, for a $\text{Zr}_{53.8}\text{Cu}_{31.6}\text{Ag}_{7.0}\text{Al}_{7.6}$ BMG (2 mm in thickness) with large bending and compressive plastic strain, the presence of heterogeneities was ruled out through Transmission Electron Microscopy (TEM), APT and anomalous small-angle X-ray scattering investigations [7]. Heterogeneities on the atomic scale in liquid and glassy $\text{Cu}_{45}\text{Zr}_{45}\text{Ag}_{10}$ were concluded from molecular dynamics simulations [11]. The model structure consists of Zr-rich clusters centred by paired and stringed Ag atoms and Cu-rich icosahedra centred by Cu, which give rise to slow-dynamics regions and improved glass-forming ability due to the Ag addition [12]. From thermodynamics point of view, Ag and Cu have positive enthalpy of mixing ($\Delta H_{\text{mix}} = +2\text{ kJ/mole}$) and as consequence a miscibility gap exists in the metastable undercooled liquid of the binary Ag–Cu system. According to the thermodynamic assessments of the ternary Ag–Cu–Zr phase diagram [13,14], an extended miscibility gap exists in the equilibrium liquid. Fig. 1 shows a calculated section of the Ag–Cu–Zr phase diagram along $(\text{Cu}_{0.5}\text{Zr}_{0.5})_{100-x}\text{Ag}_x$ using the data given in [13]. A stable miscibility gap of the liquid occurs in the range from about $x = 35\text{ at.}\%$ Ag to

* Corresponding author. Tel.: +49 3514659367.

E-mail address: n.mattern@ifw-dresden.de (N. Mattern).

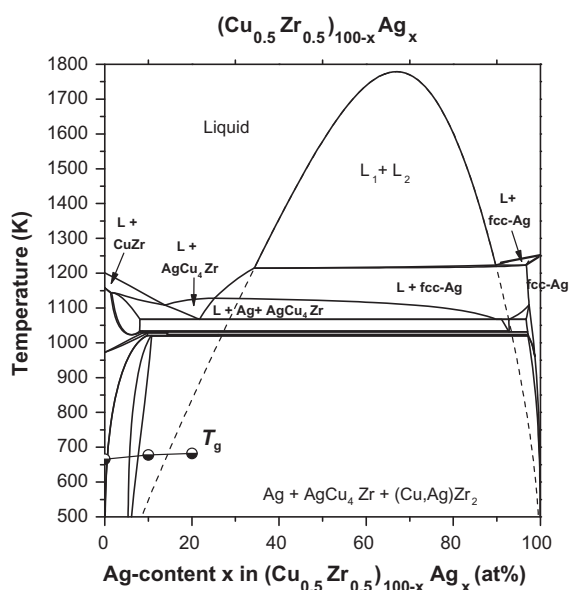


Fig. 1. Calculated section of the Ag–Cu–Zr phase diagram along CuZr–Ag. Primary phase fields are indicated. Metastable extension of the miscibility gap of melt is given by the dotted line. Glass transition temperatures of $(\text{CuZr})_{100-x}\text{Ag}_x$ glasses ($x = 0, 10, 20$) are given by the data points.

90 at.% Ag. For lower Ag-content ($25 \leq x \leq 35$ at.%) primary crystallisation of *fcc*-Ag should proceed upon cooling the melt. However, in the case of metastable undercooling phase separation could take place also for $15 \leq x \leq 35$ at.% Ag as can be seen by the extrapolation of the binodal line in Fig. 1 (dotted line). Because the glass transition temperature T_g of a $\text{Cu}_{40}\text{Zr}_{40}\text{Ag}_{20}$ alloy (T_g is given by points in Fig. 1) is below the binodal line, the phase-separated liquid would be frozen into a heterogeneous glass, whereas for the $\text{Cu}_{45}\text{Zr}_{45}\text{Ag}_{10}$ alloy a homogeneous glass would be expected. Experimental investigation of the Ag–Cu–Zr phase diagram had confirmed the presence of a miscibility gap in the liquid phase by the analysis of the microstructure of cast alloys melts [15–19]. However, for rapidly quenched Cu–Zr–Ag ribbons it was concluded that the experimentally determined glass forming composition range overlaps marginally with the calculated miscibility gap [15].

The aim of this work was to investigate the influence of composition and quenching rate on the microstructure of $(\text{CuZr})_{100-x}\text{Ag}_x$ alloys with special attention to the occurrence of phase separation. We will show that the glasses with $x \leq 20$ at.% Ag are homogeneous and glass–crystal composite are formed for $x = 30$ –40 at.% Ag by primary crystallization of *fcc*-Ag upon quenching the melt.

2. Experimental details

$(\text{Cu}_{0.5}\text{Zr}_{0.5})_{100-x}\text{Ag}_x$ ($x = 0, 10, 20, 30, 35$ and 40 at.% Ag) ingots were prepared by arc melting of high-purity elements (99.9%) under argon atmosphere. In order to ensure efficient mixing, the ingots were re-melted at least three times. Rapidly quenched ribbon samples of the alloys were fabricated by single-roller melt spinning using a quartz crucible and a wheel speed of 30 ms^{-1} . The casting temperature was about $T = 1650 \text{ K}$. The resulting ribbons had a width of 4 mm and a thickness of about 40 μm . Bulk rod samples of 5 mm in diameter and 50 mm in length were prepared by suction casting from pre-alloys for $x = 30, 35$ and 40 at.% Ag. The structures of the samples were characterized by X-ray diffraction (XRD: Panalytical X'pert Pro) with $\text{Co K}\alpha$ radiation. Highlights. Differential scanning calorimetry (DSC) was performed employing a Diamond DSC (Perkin–Elmer) with a heating rate of 40 K min^{-1} . The glass transition temperature T_g and the crystallization temperature T_x were determined as the on-set of the respective events, using the two-tangents method. Microstructure investigations were carried out with a scanning electron microscope (SEM: Zeiss Gemini 1530) and Transmission Electron Microscope (TEM: JEOL 2100F) operated at 200 kV. The thin-foil samples for TEM investigations were prepared by using an ion milling system (Gatan, Model PIPS 691) with liquid

nitrogen cooling. A dual-beam focused-ion beam system (FEI Helios Nanolab 600i) was used for the fabrication of the Atom Probe Tomography (APT) tips. The APT specimens were analyzed using the local electrode atom probe (LEAP 3000 X HR™) equipped with diode-pumped solid-state laser operating at the second harmonic frequency of 532 nm with a pulse duration of $\sim 10 \text{ ps}$ and a laser spot size $< 10 \mu\text{m}$. Pulse laser atom probe analyses were carried out at 60 K with 0.4 nJ pulse energy at an average detection rate of 0.005 ions/pulse. The APT data was evaluated using the software IVAS 3.6 provided by Cameca Instruments. Composition profiles with respect to distance from the Ag cluster were obtained using the proximity histogram method. An isoconcentration surface of 40 at.% Ag is utilized as a reference surface for the proxigram analysis which provided a topologically stable representation of Ag clusters when varying the isoconcentration value around 40 at.% Ag. Unless otherwise mentioned the use of isoconcentration surface in depicting Ag clusters is only used for clarity and not for quantification. When interpreting the morphology of clusters, account has to be taken for the local magnification effect owing to the fact that Ag has a lower evaporation field (24 V nm^{-1}) than Cu (30 V nm^{-1}) and Zr (28 V nm^{-1}) [20]. As a consequence, during field evaporation the Cu clusters are slightly recessed and are therefore projected at a lower magnification towards the detector compared to the matrix atoms. This results in an atomic density relatively higher in the clusters than in the matrix [21]. The slightly elongated morphology observed for some of the clusters is also due to of this effect [20]. Hence, to overcome the apparent distortions induced in the clusters the maximum-separation method of the cluster analysis with a maximum separation distance of 0.4 nm is utilized in order to estimate the size as described in Ref. [22].

3. Results and discussion

Fig. 2 shows the XRD patterns of the as-quenched ribbons with different Ag-content x . Fully glassy state were obtained for $x = 10$ and 20 at.% Ag as indicated by the diffuse diffraction maxima and by the absence of any crystalline reflections. For $x = 30$ at.% Ag, a very small fraction of *fcc*-Ag is evident beside the glassy main phase. For the ribbons $30 \leq x \leq 40$ at.% Ag the volume fraction of the *fcc*-Ag phase increases and, accordingly the glassy fraction is reduced.

The thermal behaviour of the rapidly quenched ribbons is shown in Fig. 3 by the corresponding DSC scans. The curves confirm the glassy nature for the melt spun ribbons with $0 \leq x \leq 20$. The glass transition and the crystallization events can be clearly seen by the endothermic and the exothermic event, respectively. The crystallization temperature and the range of supercooled liquid, both increase for Ag additions $x \leq 20$. The corresponding values are given in Table 1. The same trend is observed for $\text{Cu}_{55-x}\text{Zr}_{45}\text{Ag}_x$ glassy ribbons ($x = 0, 10, 20$ at.% Ag) reported in [9]. The increased thermal stability of the Cu–Zr glasses by Ag-additions points to a homogeneous element distribution in the glass, because in case of phase separation the opposite behaviour should occur. For the alloys with $x \geq 30$ at.% Ag the crystallization

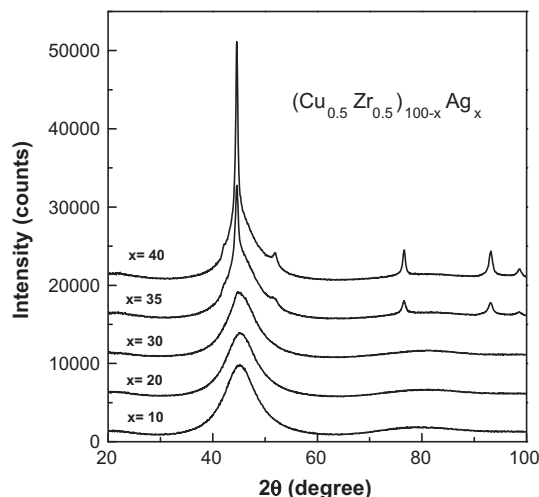


Fig. 2. XRD patterns of rapidly quenched $(\text{Cu}_{0.5}\text{Zr}_{0.5})_{100-x}\text{Ag}_x$ ribbons.

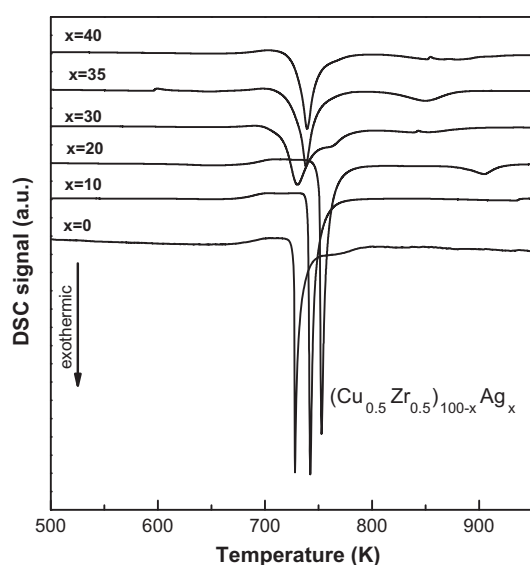


Fig. 3. DSC scans of rapidly quenched $(\text{Cu}_{0.5}\text{Zr}_{0.5})_{100-x}\text{Ag}_x$ ribbons (heating rate was 40 K/min).

Table 1

Glass transition temperature, crystallization temperature and crystallization enthalpy of rapidly quenched $(\text{Cu}_{0.5}\text{Zr}_{0.5})_{100-x}\text{Ag}_x$ ribbons determined from DSC data (40 K/min heating rate).

$x - \text{Ag (at.\%)}$	Thermal properties		
	T_g (K)	T_x (K)	ΔH (J/g)
0	676	717	−49.6
10	678	740	−75.5
20	683	751	−78.7
30	663	720	−72.5
35	681	729	−58.6
40	678	730	−56.3

of the remaining amorphous phase is slightly shifted to a lower temperature. The transformation enthalpy as determined from the area of the exothermic peak is also reduced due to the smaller fraction of glassy phase in accordance with the XRD results. The formed crystalline phases after heat treatment were identified from XRD measurements (not shown here). The corresponding results are presented in Table 2. The experimentally observed phase compositions after annealing at $T = 973$ K were found to be in accordance with the results of phase diagram calculation (Table 2).

Based on the XRD results the fully amorphous ribbons ($x = 10, 20$) and the amorphous matrix composite ribbons with low fraction of fcc-Ag ($x = 30, 35$) were chosen for further analysis by TEM. Fig. 4(a) and (b) shows high resolution (HR-TEM) images of the as-quenched state of $x = 10$ and 20 at.% Ag ribbon samples. The amorphous structure is confirmed by the absence of any

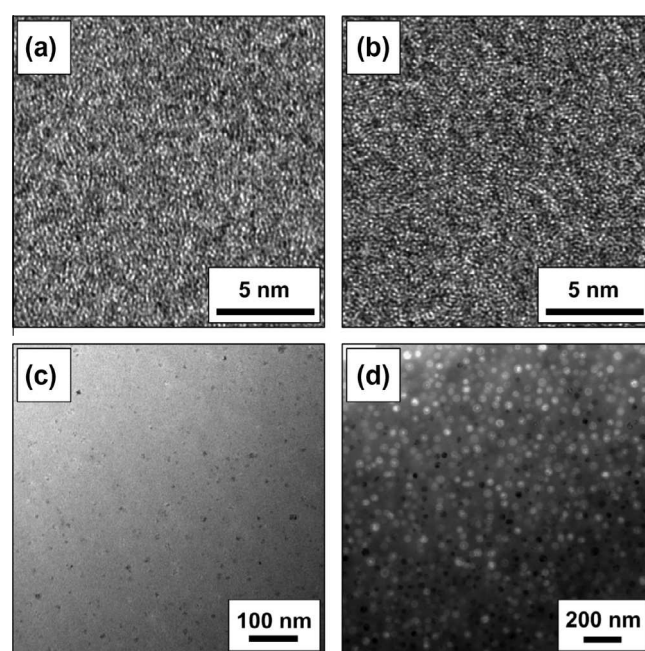


Fig. 4. TEM images of rapidly quenched $(\text{Cu}_{0.5}\text{Zr}_{0.5})_{100-x}\text{Ag}_x$ ribbons with different Ag-content x . (a) $x = 10$; (b) $x = 20$; (c) $x = 30$ and (d) $x = 35$ at.%. Fully glassy structures are obtained for $x = 10, 20$ at.% Ag. Composite structure consisting of Ag nanocrystals and amorphous matrix phase for $x = 30, 35$.

ordered contrast in the HR-TEM images. For the as-quenched sample with $x = 30$ at.% Ag, the bright field (BF) TEM image in Fig. 4(c) clearly reveals the presence of Ag crystallites with the size of about 5 nm embedded in the amorphous matrix. For the ribbon sample with $x = 35$ at.% Ag, the presence of higher volume fraction of Ag crystallites with the size of about 20 nm can be noticed from the BF TEM image shown in Fig. 4(d).

In order to analyse the presence of heterogeneities on the nano-scale, ATP investigations were performed for selected glassy and partly nanocrystalline samples according to XRD and TEM results. The resulting spatial element distributions of the as-quenched ribbons with $x = 20, 30$ and 35 at.% Ag are shown in Fig. 5(a–c). For the rapidly quenched sample with $x = 20$ at.% Ag a homogeneous distribution of Ag and all the other elements is observed (Fig. 5a). The binomial distribution of the concentration fluctuations as shown in Fig. 5(d) confirms the absence of any phase separation. The degree of randomness is measured by the parameter μ . The value ranges between 0 and 1, where 0 stands for complete randomness and 1 indicates solute clustering or deviation from randomness [23]. As shown in Fig. 5(d), the experimentally obtained frequency distribution of Ag is in good agreement with the corresponding theoretical binomial distribution of a random solid solution with a minimum μ value of 0.0553 indicating complete randomness. It should be noted that the atomic scale heterogeneities found by MD simulations in [10] are below the spatial

Table 2

Phase compositions of $(\text{Cu}_{0.5}\text{Zr}_{0.5})_{100-x}\text{Ag}_x$ ribbons and rods in the as-prepared and annealed state. The phase compositions from the CALPHAD calculation is given for comparison.

Ag (at.%)	r.q. ribbons		Cast rods (5 mm in diameter)		CALPHAD $T = 973$ K
	As-quenched	Annealed at $T = 973$ K	As-cast	Annealed at $T = 973$ K	
0	Amorphous	$\text{Cu}_{10}\text{Zr}_7 + \text{CuZr}_2$	–	–	$\text{Cu}_{10}\text{Zr}_7 + \text{CuZr}_2$
10	Amorphous	$\text{Cu}_{10}\text{Zr}_7 + (\text{Cu,Ag})\text{Zr}$	–	–	$\text{Cu}_{10}\text{Zr}_7 + (\text{Cu,Ag})\text{Zr}$
20	Amorphous	$\text{Cu}_{10}\text{Zr}_7 + (\text{Cu,Ag})\text{Zr} + \text{AgCu}_4\text{Zr}$	–	–	$\text{AgCu}_4\text{Zr} + (\text{Cu,Ag})\text{Zr}$
30	Amorphous + Ag	$\text{Ag} + \text{AgCu}_4\text{Zr} (\text{Cu,Ag})\text{Zr}$	$\text{Ag} + \text{AgCu}_4\text{Zr} (\text{Cu,Ag})\text{Zr} + \text{Cu}_{10}\text{Zr}_7$	$\text{Ag} + \text{AgCu}_4\text{Zr} + (\text{Cu,Ag})\text{Zr}$	$\text{Ag} + \text{AgCu}_4\text{Zr} + (\text{Cu,Ag})\text{Zr}$
35	Amorphous + Ag	$\text{Ag} + \text{AgCu}_4\text{Zr} (\text{Cu,Ag})\text{Zr}$	$\text{Ag} + \text{AgCu}_4\text{Zr} (\text{Cu,Ag})\text{Zr} + \text{Cu}_{10}\text{Zr}_7$	$\text{Ag} + \text{AgCu}_4\text{Zr} + (\text{Cu,Ag})\text{Zr}$	$\text{Ag} + \text{AgCu}_4\text{Zr} (\text{Cu,Ag})\text{Zr}$
40	Amorphous + Ag	$\text{Ag} + \text{AgCu}_4\text{Zr} (\text{Cu,Ag})\text{Zr}$	$\text{Ag} + \text{AgCu}_4\text{Zr} (\text{Cu,Ag})\text{Zr} + \text{CuZr}$	$\text{Ag} + \text{AgCu}_4\text{Zr} + (\text{Cu,Ag})\text{Zr}$	$\text{Ag} + \text{AgCu}_4\text{Zr} (\text{Cu,Ag})\text{Zr}$

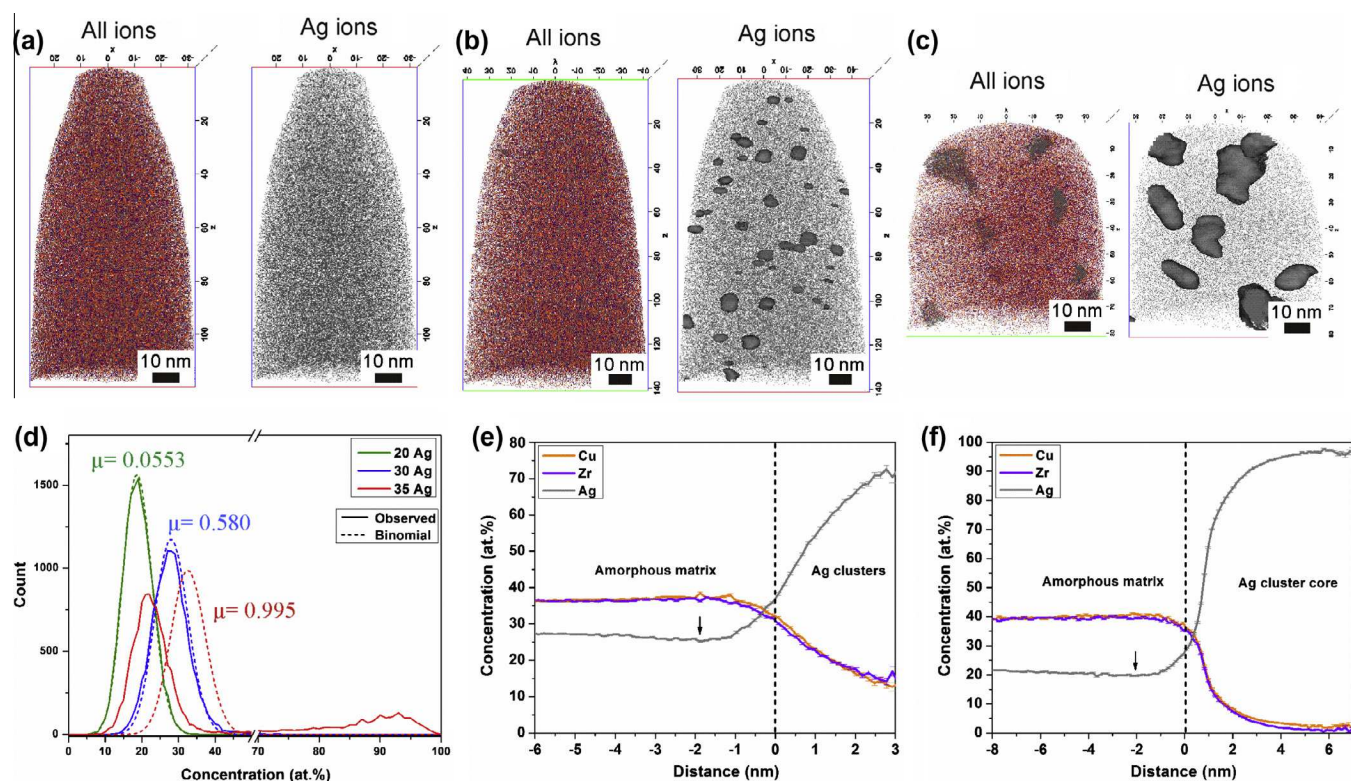


Fig. 5. Spatial arrangement of all the atoms and Ag-atoms with clusters in terms of isoconcentration surfaces (40 at.% Ag interface) of rapidly quenched $(\text{Cu}_{0.5}\text{Zr}_{0.5})_{100-x}\text{Ag}_x$ ribbons by ATP. (a) $x=20$; (b) $x=30$; (c) $x=35$; (d) binomial frequency distribution analysis of Ag atoms with 100 atoms per bin to verify homogeneity; (e) and (f) proximity histograms of 0.15 nm bin size with respect to all the Ag clusters in the analyzed volume of (b) and (c) for $x=30$ and 35 samples, respectively.

resolution of the ATP technique. The alloy with 30 at.% Ag clearly shows a heterogeneous concentration distribution in Fig. 5(d) by a shift of the experimentally observed distribution resulting in a significantly higher μ value. In order to elaborate the Ag-rich clusters isoconcentration surfaces of 40 at.% Ag are drawn as shown in Fig. 5(b). According to the XRD and TEM results, the clusters are the Ag nanocrystals and the average size of about 5 nm agrees well with the TEM images. The Ag concentration within the nanocrystals is about ~75 at.% as obtained from the statistical proximity histogram (inclusive of at least 50 Ag clusters) of Fig. 5(e) with equal partitioning of Cu and Zr. The chemical composition of the glassy phase is about $\text{Cu}_{36.5}\text{Zr}_{36.5}\text{Ag}_{27}$. A slight depletion of Ag concentration along the interface region between the Ag clusters and the surrounding amorphous matrix is noticed. The Ag depleted interface region is indicated by an arrow in Fig. 5(e). Such depletion can be attributed to the diffusion controlled crystal growth, wherein, Ag atoms from the surrounding amorphous regions diffuse to the Ag-rich nanocrystals. For the case of the rapidly quenched sample with 35 at.% Ag we observe coarsened heterogeneities (Fig. 5c). The Ag-rich clusters (nanocrystals) distinguished by dark isoconcentration surfaces of 40 at.% Ag own a size of about 15 nm. Fig. 5(f) shows the composition of the surrounding phase which corresponds to the remaining glassy main phase of about $\text{Cu}_{40}\text{Zr}_{40}\text{Ag}_{20}$. Ag depletion along the interface region is also noticed (indicated by arrow in Fig. 5(f)). The concentration inside the clusters in this case was ~95 at.% Ag which is also confirmed from the binomial distribution shown in Fig. 5(d) where the experimentally observed distribution shows a peak near the mean concentration of 95 at.% Ag.

From the experimental results it follows that there is no indication of phase separation for CuZr-Ag glasses with 10 and 20 at.% Ag. The maximum of Ag addition to CuZr is about 20 at.% in order to obtain a metallic glass by melt spinning. The composition

dependence of the glass forming ability of CuZr-Ag alloys is in good agreement with results reported in [9] and as pointed out can be understood by the T_g/T_{liquidus} criteria [24]. The addition of Ag reduces the liquidus temperature T_{liquidus} of CuZr up to about 10 at.% as can be seen in Fig. 1. The increase of T_{liquidus} for $x > 12$ at.% reduces the glass forming ability and leads to the formation of glass-crystal composites by primary formation of Ag during quenching the melt. Due to the precipitation of Ag crystals the liquid phase becomes altered in chemical composition and when the Ag-content reaches about 20 at.%, the remaining liquid is quenched into the glassy phase.

These experimental observations are in contrast to the reported extension of the liquid miscibility gap of the ternary Ag-Cu-Zr system [13–19]. Therefore, the microstructure of cast rods for alloys with $x=30$ –40 at.% Ag were investigated in order to clarify this contradiction. Fig. 6 shows the corresponding SEM images of the representative microstructures. The cast rods are fully crystalline. The phase compositions according to the XRD analysis are given in Table 2. The SEM images exhibit the solidification behaviour of the alloys upon casting the melt. For all compositions Ag-dendrites (white) are formed as the primary phase from the homogeneous liquid. As the second stage of crystallization the (Ag,Cu)Zr phase is formed (gray, needle like) from the CuZr-rich liquid. About 15 at.% Cu are solved in the AgZr phase as determined by the EDX analysis. The matrix phase (dark) has a composition of about $\text{Cu}_{43}\text{Zr}_{35}\text{Ag}_{22}$ and consists of a eutectic like microstructure, which can not be resolved by EDX in the SEM. In the XRD patterns we observe beside Ag and (Ag,Cu)Zr the ternary phase AgCu_4Zr as well as $\text{Cu}_{10}\text{Zr}_7$ or CuZr. The cast rods do not represent the equilibrium state. After annealing the rods at $T=973$ K the phase compositions are in accordance with the phase diagram calculations (Table 2). According to the phase diagram shown in Fig. 1 such a primary crystallization of Ag should occur only for the alloy with

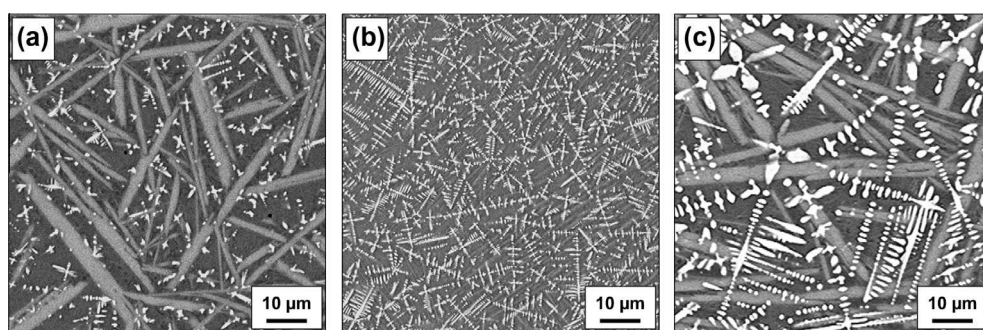


Fig. 6. SEM images of $(\text{Cu}_{0.5}\text{Zr}_{0.5})_{100-x}\text{Ag}_x$ cast rods. (a) $x = 30$; (b) $x = 35$; (c) $x = 40$.

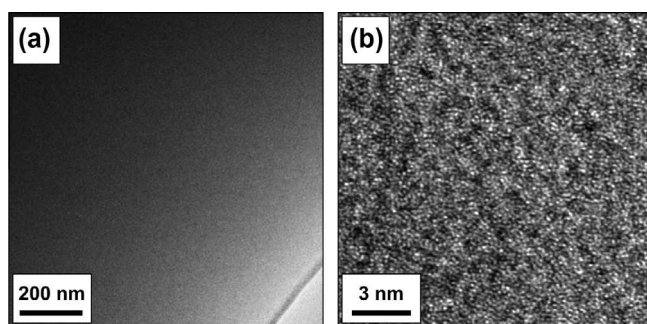


Fig. 7. TEM images of r.q. $\text{Cu}_{40}\text{Zr}_{40}\text{Al}_{10}\text{Ag}_{10}$ (a) bright field image and (b) high resolution image.

$x = 30$ at.% Ag. On the other side, the SEM observations of the cast rods are in accordance with the obtained results for the rapidly quenched ribbons. This means, that the miscibility gap in the liquid phase is less extended to the Ag-poor side and the calculated binodal line (along the $\text{Cu}_{0.5}\text{Zr}_{0.5}$ –Ag section in Fig. 1) has to be shifted to higher Ag contents ($x > 40$ at.% Ag). Then, this would also explain why no phase separation occurs in the $\text{Cu}_{40}\text{Zr}_{40}\text{Ag}_{20}$ glass.

Because phase separation was reported for $\text{Cu}_{43}\text{Zr}_{43}\text{Al}_7\text{Ag}_7$ BMG bulk metallic glass [8], we also analysed the microstructure of a $\text{Cu}_{40}\text{Zr}_{40}\text{Al}_{10}\text{Ag}_{10}$ rapidly quenched ribbon. Since the ternary $\text{Cu}_{40}\text{Zr}_{40}\text{Ag}_{20}$ glass does not show phase separation, there is no reason from thermodynamics point of view to have this in the quaternary glass. This expectation was confirmed by the TEM

and APT investigations. Fig. 7 shows the TEM images of rapidly quenched $\text{Cu}_{40}\text{Zr}_{40}\text{Al}_{10}\text{Ag}_{10}$. Both, the BF (Fig. 7a) and HR TEM (Fig. 7b) images give evidence of homogeneous glassy structure. The APT results are shown in Fig. 8. The spatial arrangements of all elements and Ag atoms separately in Fig. 8(a) demonstrates the presence of a homogeneous structure without any indication of heterogeneities. Similar to the $\text{Cu}_{40}\text{Zr}_{40}\text{Ag}_{20}$ glass, the experimentally observed frequency distribution for all the constituent elements is in good agreement with the theoretical distribution. For Ag, the χ^2 value, the degree of freedom (n_d) and the significance probability (p -value) are given in Fig. 8(b). Considerably high p -value and the minimum of μ value, close to zero confirm the homogeneous distribution of Ag.

4. Conclusions

Metallic glasses can be prepared by melt-spinning of $(\text{Cu}_{0.5}\text{Zr}_{0.5})_{100-x}\text{Ag}_x$ up to $x = 20$ at.% Ag. These metallic glasses are characterized by a homogeneous microstructure without any indication of phase separation. The same is true for the quaternary $\text{Cu}_{40}\text{Zr}_{40}\text{Al}_{10}\text{Ag}_{10}$ glass. For higher contents $30 \leq x \leq 40$ at.% Ag composite structures are obtained consisting of fcc -Ag nanocrystallites and remaining glassy matrix phase with a composition of about $\text{Cu}_{40}\text{Zr}_{40}\text{Ag}_{20}$. The structure formation upon quenching the melt for $30 \leq x \leq 40$ at.% Ag is determined by the primary formation of fcc -Ag phase rather than liquid phase separation. The current thermodynamic assessments of the literature overestimate the miscibility gap of the liquid phase. A re-assessment of the Ag–Cu–Zr system is required in order to clarify the contradictions.

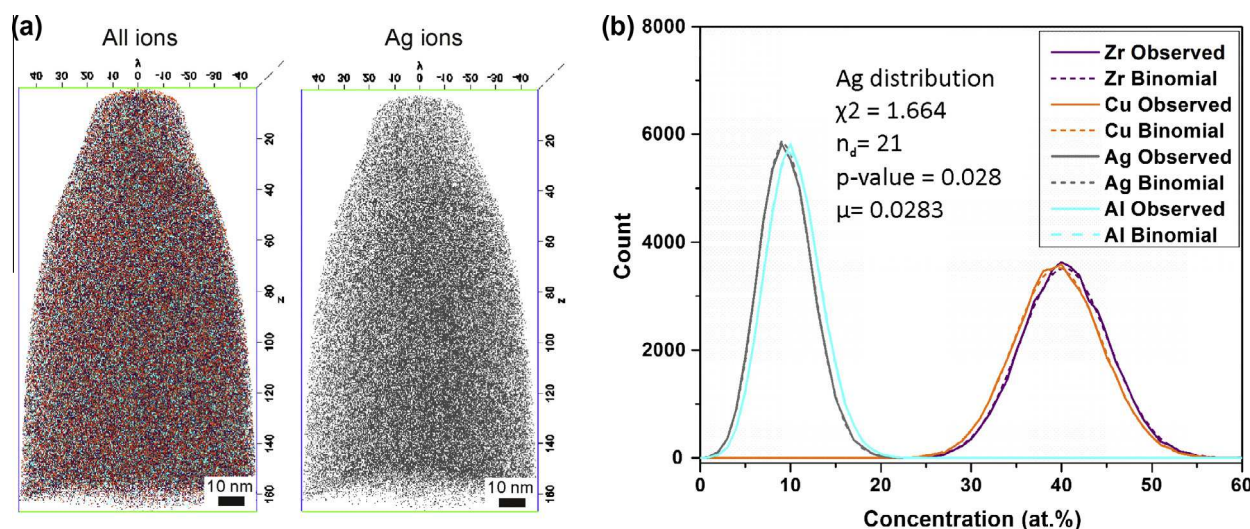


Fig. 8. APT results of r.q. $\text{Cu}_{40}\text{Zr}_{40}\text{Al}_{10}\text{Ag}_{10}$. (a) Spatial distribution of all the atoms of $\text{Cu}_{40}\text{Zr}_{40}\text{Al}_{10}\text{Ag}_{10}$ and (b) Ag-atoms only. Binomial frequency distribution analysis of Ag atoms with 100 atoms per bin to verify homogeneity.

Acknowledgements

The authors thank B. Bartusch and B. Opitz for technical assistance. Valuable discussions with O. Fabrichnaya and D. Louzguine are gratefully acknowledged. This work was supported by the Global Research Laboratory (GRL) Program of the Korea Ministry of Education, Science and Technology. Financial support of Tohoku University Sendai is acknowledged for research stay at the Institute for Materials Research (N.M.).

References

- [1] A. Inoue, A. Takeuchi, *Acta Mater.* 59 (2011) 2243.
- [2] D.S. Sung, O.J. Kwon, E. Fleury, K.B. Kim, J.C. Lee, D.H. Kim, Y.C. Kim, *Met. Mater. Int.* 10 (2004) 575.
- [3] Q.S. Zhang, W. Zhang, A. Inoue, *Scripta Mater.* 55 (2006) 711.
- [4] Q.K. Jiang, X.D. Wang, X.P. Nie, G.Q. Zhang, H. Ma, H.-J. Fecht, J. Bendnarcik, H. Franz, Y.G. Liu, Q.P. Cao, J.Z. Jiang, *Acta Mater.* 56 (2008) 1785.
- [5] W. Zhang, A. Inoue, *J. Mater. Res.* 21 (2006) 234.
- [6] K.K. Song, P. Gargarella, S. Pauly, G.Z. Ma, U. Kühn, J. Eckert, *J. Appl. Phys.* 112 (2012) 063503.
- [7] Q.P. Cao, Y.M. Chen, K. Hono, C. Zhong, Q.K. Jiang, X.P. Nie, L.Y. Chen, X.D. Wang, J.Z. Jiang, *Acta Mater.* 59 (2011) 1037.
- [8] J.C. Oh, T. Ohkubo, Y.C. Kim, E. Fleury, K. Hono, *Scripta Mater.* 53 (2005) 165.
- [9] D.V. Louzguine-Luzgin, G. Xie, W. Zhang, A. Inoue, *Mater. Sci. Eng. A* 456 (2007) 146.
- [10] D.V. Louzguine-Luzgin, T. Wada, H. Kato, J. Perepezko, A. Inoue, *Intermetallics* 18 (2010) 1235.
- [11] T. Fujita, K. Konno, W. Zhang, V. Kumar, M. Matsuura, A. Inoue, T. Sakurai, M.W. Chen, *Phys. Rev. Lett.* 103 (2009) 075502.
- [12] T. Fujita, P.F. Guan, H.W. Sheng, A. Inoue, T. Sakurai, M.W. Chen, *Phys. Rev. B* 81 (2010) 140204(R).
- [13] X.C. He, H. Wang, H.S. Liu, Z.P. Jin, *Calphad* 30 (2006) 367.
- [14] D.H. Kang, I.H. Jung, *Intermetallics* 18 (2010) 815.
- [15] A.A. Kündig, M. Ohnuma, T. Ohkubo, T. Abe, K. Hono, *Scripta Mater.* 55 (2006) 449.
- [16] A. Castellero, D.H. Kang, I.H. Jung, G. Angella, M. Vedani, M. Baricco, *J. Alloys Comp.* 536 (2012) 148.
- [17] D. Janovszky, K. Tomolya, A. Sycheva, G. Kaptay, *J. Alloys Comp.* 541 (2012) 353.
- [18] D. Janovszky, K. Tomolya, A. Sycheva, P. Pekker, A. Roósz, *J. Alloys Comp.* 586 (2014) 194.
- [19] K. Tomolya, D. Janovszky, A. Sycheva, M. Benke, C. Erdohegyi, A. Roosz, *J. Alloys Comp.* 586 (2014) 184.
- [20] M.K. Miller, A. Cerezo, A. M.G. Hetherington, G.D.W. Smith, *Atom Probe Field Ion Microscopy*, Clarendon Press, 1996.
- [21] F. Vurpillot, A. Bostel, D. Blavette, *Appl. Phys. Lett.* 76 (2000) 3127.
- [22] D. Isheim, M.S. Gagliano, M.E. Fine, D.N. Seidman, *Acta Mater.* 54 (2006) 841.
- [23] M.P. Moody, L.T. Stephenson, A.V. Ceguerra, S.P. Ringer, *Microscopy Res. Tech.* 71 (2008) 542.
- [24] T. Turnbull, M.H. Cohen, *J. Chem. Phys.* 34 (1961) 120.